catalysts

MDPI

Article

Comprehensive Comparison between Nanocatalysts of Mn−Co/TiO_2 and Mn−Fe/TiO_2 for NO Catalytic Conversion: An Insight from Nanostructure, Performance, Kinetics, and Thermodynamics

Yan Gao [1,2,*], Tao Luan [3], Shitao Zhang [2], Wenchao Jiang [2], Wenchen Feng [3] and Haolin Jiang [3]

1 Key Laboratory of Renewable Energy Building Application Technology of Shandong Province, Shandong Jianzhu University, Jinan 250101, China

2 Department of Thermal Engineering, Shandong Jianzhu University, Jinan 250101, China; shitao_zhang@hotmail.com (S.Z.); jiang_wc@126.com (W.J.)

3 Engineering Laboratory of Power Plant Thermal System Energy Saving of Shandong Province, Shandong University, Jinan 250061, China; prof.luantao@gmail.com (T.L.); wcfeng18@126.com (W.F.); haolin_jiang@hotmail.com (H.J.)

* Correspondence: gaoyan.sdu@hotmail.com; Tel.: +86-138-6415-4887

Received: 15 January 2019; Accepted: 9 February 2019; Published: 13 February 2019

Abstract: The nanocatalysts of Mn−Co/TiO_2 and Mn−Fe/TiO_2 were synthesized by hydrothermal method and comprehensively compared from nanostructures, catalytic performance, kinetics, and thermodynamics. The physicochemical properties of the nanocatalysts were analyzed by N_2 adsorption, transmission electron microscope (TEM), X-ray diffraction (XRD), H_2-temperature-programmed reduction (TPR), NH_3-temperature-programmed desorption (TPD), and X-ray photoelectron spectroscopy (XPS). Based on the multiple characterizations performed on Mn−Co/TiO_2 and Mn−Fe/TiO_2 nanocatalysts, it can be confirmed that the catalytic properties were decidedly dependent on the phase compositions of the nanocatalysts. The Mn−Co/TiO_2 sample presented superior structure characteristics than Mn−Fe/TiO_2, with the increased surface area, the promoted active components distribution, the diminished crystallinity, and the reduced nanoparticle size. Meanwhile, the Mn^{4+}/Mn^{n+} ratios in the Mn−Co/TiO_2 nanocatalyst were higher than Mn−Fe/TiO_2, which further confirmed the better oxidation ability and the larger amount of Lewis acid sites and Bronsted acid sites on the sample surface. Compared to Mn−Fe/TiO_2 nanocatalyst, Mn−Co/TiO_2 nanocatalyst displayed the preferable catalytic property with higher catalytic activity and stronger selectivity in the temperature range of 75–250 °C. The results of mechanism and kinetic study showed that both Eley-Rideal mechanism and Langmuir-Hinshelwood mechanism reactions contributed to selective catalytic reduction of NO with NH_3 (NH_3-SCR) over Mn−Fe/TiO_2 and Mn−Co/TiO_2 nanocatalysts. In this test condition, the NO conversion rate of Mn−Co/TiO_2 nanocatalyst was always higher than that of Mn−Fe/TiO_2. Furthermore, comparing the reaction between doping transition metal oxides and NH_3, the order of temperature−Gibbs free energy under the same reaction temperature is as follows: $Co_3O_4 < CoO < Fe_2O_3 < Fe_3O_4$, which was exactly consistent with nanostructure characterization and NH_3-SCR performance. Meanwhile, the activity difference of MnO_x exhibited in reducibility properties and Ellingham Diagrams manifested the promotion effects of cobalt and iron dopings. Generally, it might offer a theoretical method to select superior doping metal oxides for NO conversion by comprehensive comparing the catalytic performance with the insight from nanostructure, catalytic performance, reaction kinetics, and thermodynamics.

Keywords: NH_3-SCR; nanostructure; kinetics; thermodynamics; manganese oxides

1. Introduction

Nitrogen oxides (NO_x) generated from fossil fuels are regarded as the primary reason for acid rain, ozone depletion, photochemical smog, and greenhouse effects [1]. Selective catalytic reduction of NO_x with NH_3 or urea as a reductant (NH_3-SCR) is proposed to be the most efficient method for eliminating NO_x from stationary source and mobile source [2]. In recent decades, the commercial catalyst of V_2O_5-$WO_3(MoO_3)/TiO_2$ used for NH_3-SCR process exhibited an excellent catalytic property in the typical standard SCR reaction within the temperature range of 300–400 °C [3,4].

$$4NO + 4NH_3 + O_2 \rightarrow 4N_2 + 6H_2O \quad (1)$$

Nowadays, for the purpose of reducing the inhibiting effects of ash and SO_2 over the SCR catalysts, there is an intense interest in developing catalysts for NO reduction at lower temperature [5]. However, the $V_2O_5-WO_3(MoO_3)/TiO_2$ catalysts demand a strict temperature window, which limits their arrangement flexibility. The vanadium-based catalysts cannot reach satisfactory efficiency of eliminating NO_x as the reaction temperature lower than 250 °C. Hence, the catalysts appropriate to low temperature SCR are strongly desired, which could be placed at the downstream of electrostatic precipitator and desulfurizer [6]. A great deal of catalysts comprised of different transition metal oxides on various supports were analyzed to improve the catalytic ability for low-temperature deNO_x. The typical transition metals, such as Mn [7], Co [8], Fe [9], Ni [10], Zn [11], and Cr [9], were well-reported to display satisfactory properties at the low temperature. Among the various transition metal elements applied in the catalysts for NO_x reduction, manganese oxides display superior activity especially at the low temperature, which can be attributed to the various types of labile oxygen and high mobility of valence states [12]. Meanwhile, it was found that cobalt and iron species can combine with manganese to produce mixed nanoparticle-oxides and exhibit high SCR activity and excellent N_2 selectivity with a wide temperature window from 100—300 °C [13,14]. These mixed nanoparticle-oxides contain abundant oxygen vacancies on the catalyst surface, forming strong interaction bands at atomic scale, such as Mn-O-Fe [15,16] and Mn-O-Co [17]. Meanwhile, the active metal species of CoO_x and FeO_x are also regarded as the typical promoters for NO_x conversion, which serve as core catalyst components of active metal oxides, supplying surface oxygen to accelerate NO_x elimination [17,18].

Another crucial field of the investigation on NH_3-SCR process is the reaction mechanism on the active sites with a better understanding of the surface chemistry and developed kinetic models to evaluate the reactions. It was widely accepted that the main reaction of low temperature SCR complies with both the Eley-Rideal mechanism and Langmuir-Hinshelwood mechanism, which is further depended on the reaction temperature and the catalyst components [19,20]. According to the Eley-Rideal mechanism, the reaction occurred between NO and NH_3 (adsorbed) to generate an activated transition state and further decomposed into H_2O and N_2 [20]. Based on the Langmuir-Hinshelwood mechanism, the reaction happened between adsorbed NO and adsorbed NH_3 on the adjacent sites to form H_2O and N_2 [21]. Meanwhile, it was widely accepted that the first step in SCR was an oxidative abstraction of the hydrogen from adsorbed ammonia [22]. Therefore, oxidative NH_3 played an important part in the mechanism of NH_3-SCR, which could be evaluated by thermodynamics in details [7]. However, the comprehensive comparison of NO elimination over the nanocatalysts of $MnCoO_x$ and $MnFeO_x$ on TiO_2 support, especially with an insight from structure, performance, kinetics, and thermodynamics, has not been explored clearly.

In this study, the nanocatalysts of $Mn-Co/TiO_2$ and $Mn-Fe/TiO_2$ were synthesized by hydrothermal method. The physicochemical properties of the obtained samples were researched by SEM, BET, XRD, H2-TPR, NH3-TPD, and XPS. In the meantime, the catalytic performance comparation of $Mn-Co/TiO_2$ and $Mn-Fe/TiO_2$ nanocatalysts was investigated using kinetic and thermodynamic analysis. The purpose of this work was mean to explore a comprehensive perspective for optimizing multimetals SCR catalysts, especially for the Mn-based bimetals nanocatalysts.

2. Results and Discussions

2.1. Physicochemical Properties of the Nanocatalysts

2.1.1. TEM Analysis

The topographic characteristics and the porous structures of the Mn−Co/TiO_2 and Mn−Fe/TiO_2 nanocatalysts were collected by TEM test. As shown in Figure 1a, the most part of Mn−Co/TiO_2 nanocatalyst was formed with uniform elliptic nanoparticles with glabrous surfaces and well-proportioned size distribution and without apparent agglomeration, although there was a spot of tightly aggregated TiO_2 nanoparticles interfused into the smaller regular particles. Therefore, a distinct and unbroken mesh structure of micropore was form in Mn−Co/TiO_2 sample. However, according to the TEM images of Mn−Fe/TiO_2 nanocatalyst from Figure 1b, a noticeable augment in the particle size was observed. The nanoparticles were irregular, lots of which stacked on the nanocatalyst surface. According to Figure 1(c)(l), captured at a larger scope, it could be found that all active elements contained in Mn−Co/TiO_2 nanocatalyst were well dispersed without obvious irregular stacked particles. On the surface of Mn−Fe/TiO_2 nanocatalyst, the element of manganese appeared slight regional accumulation, which might be caused by the abundant micropore structure collapsing [23].

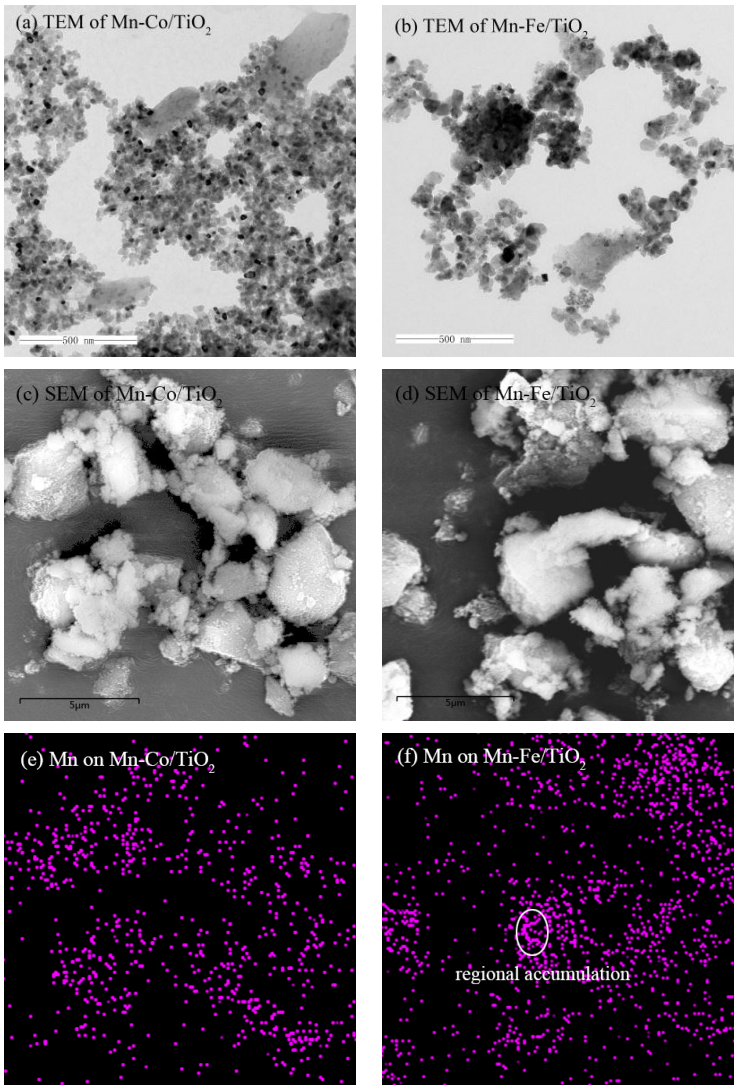

Figure 1. *Cont.*

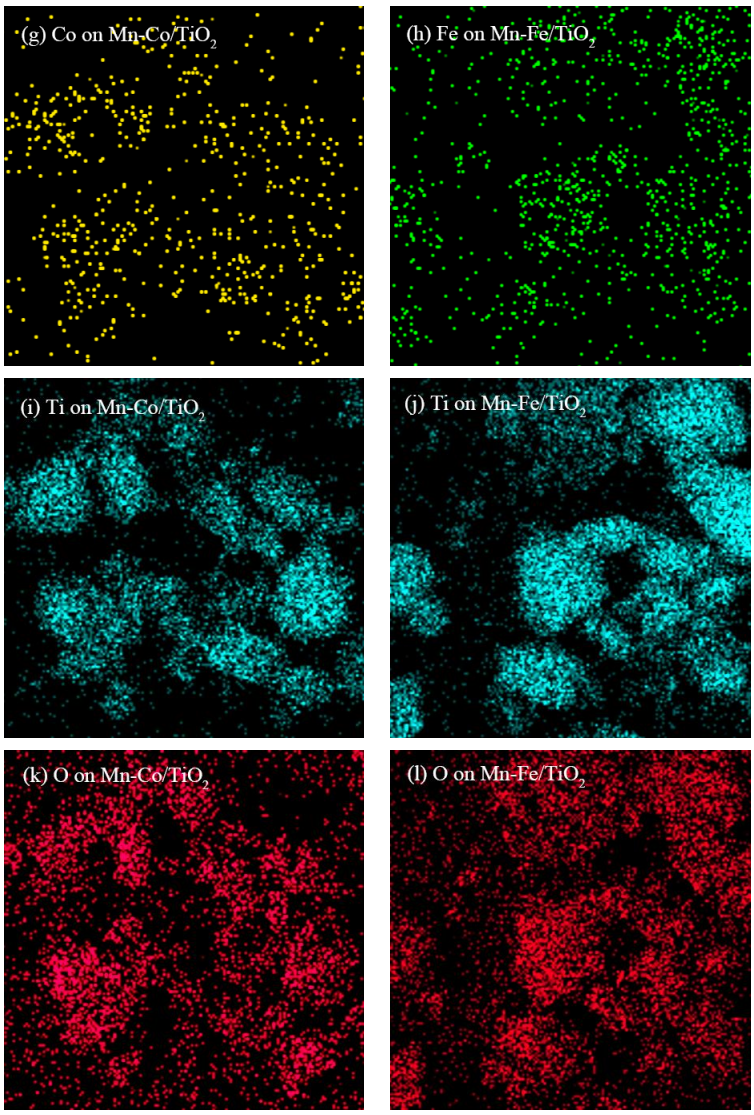

Figure 1. TEM, SEM, and Mapping of Mn−Co/TiO_2 and Mn−Co/TiO_2 nanocatalysts. (**a**) TEM of Mn−Co/TiO_2; (**b**) TEM of Mn−Fe/TiO_2; (**c**) SEM of Mn−Co/TiO_2; (**d**) SEM of Mn−Fe/TiO_2; (**e**) Mapping of Mn on Mn−Co/TiO_2; (**f**) Mapping of Mn on Mn−Fe/TiO_2; (**g**) Mapping of Co on Mn−Co/TiO_2; (**h**) Mapping of Fe on Mn−Fe/TiO_2; (**i**) Mapping of Ti on Mn−Co/TiO_2; (**j**) Mapping of Ti on Mn−Fe/TiO_2; (**k**) Mapping of O on Mn−Co/TiO_2; (**l**) Mapping of O on Mn−Fe/TiO_2.

2.1.2. BET Analysis

The structure parameters of Mn−Co/TiO_2 and Mn−Co/TiO_2 nanocatalysts, such as the specific surface areas, total pore volumes, and average pore diameters, were investigated by nitrogen-adsorption-desorption, and the test data was summarized in Table 1. Mn−Co/TiO_2 nanocatalyst attained the larger specific surface areas than Mn−Fe/TiO_2, which was possible due to the improved dispersion of $MnCoO_x$ species on the nanocatalyst surface. In the meantime, the average pore diameters increased obviously, from 33.06 nm in the Mn−Co/TiO_2 sample to 54.85 nm in the Mn−Fe/TiO_2 sample. Therefore, the $MnCoO_x$ species were more likely to promote nanocatalyst to form micropores compared with $MnFeO_x$ species [24,25]. Nevertheless, the difference of total pore volumes between Mn−Co/TiO_2 and Mn−Fe/TiO_2 nanocatalysts was not conspicuous. The total pore volumes reduced slightly from 0.531 $cm^3 \cdot g^{-1}$ in Mn−Co/TiO_2 sample to 0.424 $cm^3 \cdot g^{-1}$ in Mn−Fe/TiO_2 sample, which was probable due to the mesoporosity generation, which blocked the micropore formation, resulting in a small decrease of total pore volume. Considering the comprehensive test

results, the Mn−Co/TiO_2 nanocatalyst exhibited superior physical properties than the Mn−Fe/TiO_2 sample with higher specific surface area, larger total pore volume, and smaller average pore diameter, which were contributed to abundant micropores structures.

Table 1. Physical properties of Mn−Co/TiO_2 and Mn−Fe/TiO_2 nanocatalysts.

Samples	Specific Surface Aarea ($m^2 \cdot g^{-1}$)	Total Pore Volume ($cm^3 \cdot g^{-1}$)	Average Pore Diameter (nm)
Mn−Co/TiO_2	189.9	0.531	33.06
Mn−Fe/TiO_2	104.6	0.424	54.85

2.1.3. Components Analysis

The XRD patterns of Mn−Co/TiO_2 and Mn−Fe/TiO_2 nanocatalysts were displayed in Figure 2. The diffraction peaks for TiO_2 support contained in the nanocatalysts were preserved entirely, with the strong and distinguished reflections appearing at 2θ = 25.3°, 37.8°, 48.0°, 53.9°, 62.7°, 68.8°, 70.3°, 75.1°, and 82.7°. These accorded with the XRD pattern of anatase TiO_2 (ICDD PDF card # 71-1166) [26], with the diffraction angles of the matching peaks shifted at tiny degrees. For Mn−Co/TiO_2 nanocatalyst, each corresponding peak of anatase TiO_2 appeared at the lower diffraction angle, which indicated the interaction between $MnCoO_x$ and anatase TiO_2 was stronger than that of $MnFeO_x$ and anatase TiO_2. Meanwhile, the diffraction peaks of anatase TiO_2 in the Mn−Co/TiO_2 sample were broader and weaker than that in Mn−Fe/TiO_2 sample, which demonstrated the crystalline of anatase TiO_2 reduced with $MnCoO_x$ loading.

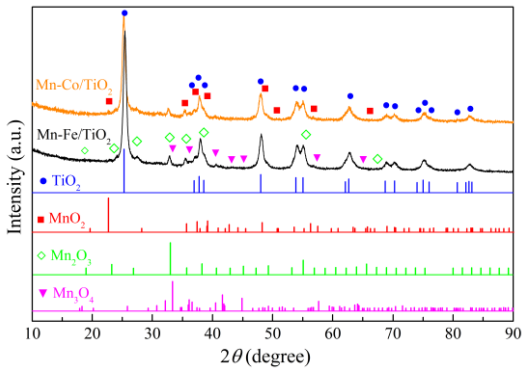

Figure 2. XRD patterns of Mn−Co/TiO_2 and Mn−Fe/TiO_2 nanocatalysts.

The diffraction peaks corresponding to MnO_x contained in Mn−Co/TiO_2 and Mn−Fe/TiO_2 nanocatalysts were very complex due to the transformation among the incomplete crystallization of manganese oxides, such as MnO_2, Mn_2O_3, Mn_3O_4, and MnO. The characterization reflections for MnO_x in the Mn−Co/TiO_2 sample were obviously weaker than that in Mn−Fe/TiO_2 sample, which manifested the active species in the Mn−Co/TiO_2 nanocatalyst, which were superior dispersed on the nanocatalyst surface or the active species incorporated into TiO_2 lattice better [27]. The diffraction peaks fitted MnO_2 (ICDD PDF card # 82-2169) precisely at about 2θ values of 22.10°, 35.19°, 36.96°, 38.72°, 47.86°, and 57.166°, which were coinciding with the crystallographic plane reflections of (110), (310), (201), (111), (311), and (420), respectively [12]. Meanwhile, both Mn−Co/TiO_2 and Mn−Fe/TiO_2 nanocatalysts exhibited the diffraction peaks corresponding to Mn_2O_3 and Mn_3O_4, apparently. The Mn_2O_3 (ICDD PDF card # 78-0390) was well-matched with intensive distinct signals at 2θ = 23.08°, 26.72°, 32.87°, and 56.89°, attributed to the crystallographic plane reflections of (211), (220), (222), and (433), respectively. The Mn_3O_4 (ICDD PDF card # 75-0765) was fitted to characteristic peaks at 36.28°, 40.67°, 41.80°, 57.73° and 64.17°, ascribed to the crystallographic plane reflections of (112), (130), (131), (115), and (063), respectively [23].

Comparing the XRD patterns of the Mn−Co/TiO_2 and Mn−Fe/TiO_2 nanocatalysts, it could be observed that the diffraction peaks of both Mn_2O_3 and Mn_3O_4 were visibly weakened in the Mn−Co/TiO_2 sample. In the meantime, the diffraction peaks of anatase TiO_2 in the Mn−Co/TiO_2 sample were also notably lower than that in Mn−Fe/TiO_2 sample. It was believed that the doping of cobalt into MnO_x obtained superior enhancement than iron on reducing the crystallization of MnO_x and TiO_2 simultaneously. Moreover, in the XRD patterns of the Mn−Co/TiO_2 nanocatalyst, there were no distinguished diffraction peaks for CoO_x, which manifested the doping of cobalt not only improved MnO_x dispersion, but also enhanced CoO_x dispersing on the nanocatalyst surface completely. The similar results were received over Mn−Fe/TiO_2 sample. Based on the phase characteristics comparation between Mn−Co/TiO_2 and Mn−Fe/TiO_2 nanocatalysts, it was believed that the Mn−Co/TiO_2 sample exhibited more excellent properties with smaller crystallinities of chemical compounds and better distribution of the active species, which were conducive to catalytic reactions.

2.1.4. Reducibility Properties

The oxidation states of the active compounds contained in nanocatalysts of Mn−Co/TiO_2 and Mn−Fe/TiO_2 were tested by H_2-TPR. The H_2 consumption curve was fitted by reduction peak separation with Gaussian function, as shown in Figure 3. The details of H_2 consumptions and reduction temperatures for each peak were listed in Table 2. In Mn−Co/TiO_2 and Mn−Fe/TiO_2 nanocatalysts, the anatase TiO_2 support did not bring remarkable reduction peaks within the test temperature range. Hence, all H_2 consumption could be attributed to the reduction process of MnO_x, CoO_x, and FeO_x. It was proposed that the typical reduction process of MnO_x contained in the nanocatalysts of Mn−Co/TiO_2 and Mn−Fe/TiO_2 complied with the following order: $MnO_2 \rightarrow Mn_2O_3$ (Mn_3O_4) $\rightarrow$MnO [28]. Mn−Co/TiO_2 nanocatalyst exhibited four reduction peaks with temperature rising from 50—850 °C, as shown in Figure 3b. The first reduction peak centered, at about 218 °C, was attributed to the high oxidation state of manganese ion converting from MnO_2 to Mn_2O_3 [29]. The dominant reduction peak (Peak 3) was caused by two sequential processes of Mn_2O_3 reducing to Mn_3O_4 and Mn_2O_3 reducing to MnO, as reported in previous literatures [12,28]. The reduction process of Mn_2O_3 to Mn_3O_4 was more liable to happen over the original amorphous Mn_2O_3 [30], while reduction process of Mn_2O_3 to MnO preferred to occur at relatively higher temperature [31]. For the Mn−Co/TiO_2 sample, the typical reduction process of cobalt oxides commonly displayed two separated peaks, the one of Co_2O_3 reducing to CoO appeared at around 327 °C, presenting as an asymmetrical reduction peak (Peak 2), the other one of CoO reducing to Co^0 occurred at about 418 °C and overlapped with MnO_x reduction peaks in whole or partly (Peak 3) [8,32]. Therefore, the fourth medium reduction peak in the Mn−Co/TiO_2 nanocatalyst was related to the reduction processes of Mn_3O_4 to MnO.

Table 2. H_2-TPR quantitative analysis of Mn−Co/TiO_2 and Mn−Fe/TiO_2 nanocatalysts.

Samples	Temperature (°C) / H_2 Consumption (mmol·g^{-1})				
	Peak 1	**Peak 2**	**Peak 3**	**Peak 4**	**Total**
Mn−Co/TiO_2	218/1.14	327/0.21	418/2.12	517/0.96	- /4.43
Mn−Fe/TiO_2	276/0.83	387/0.41	436/0.54	501/1.59	- /3.37

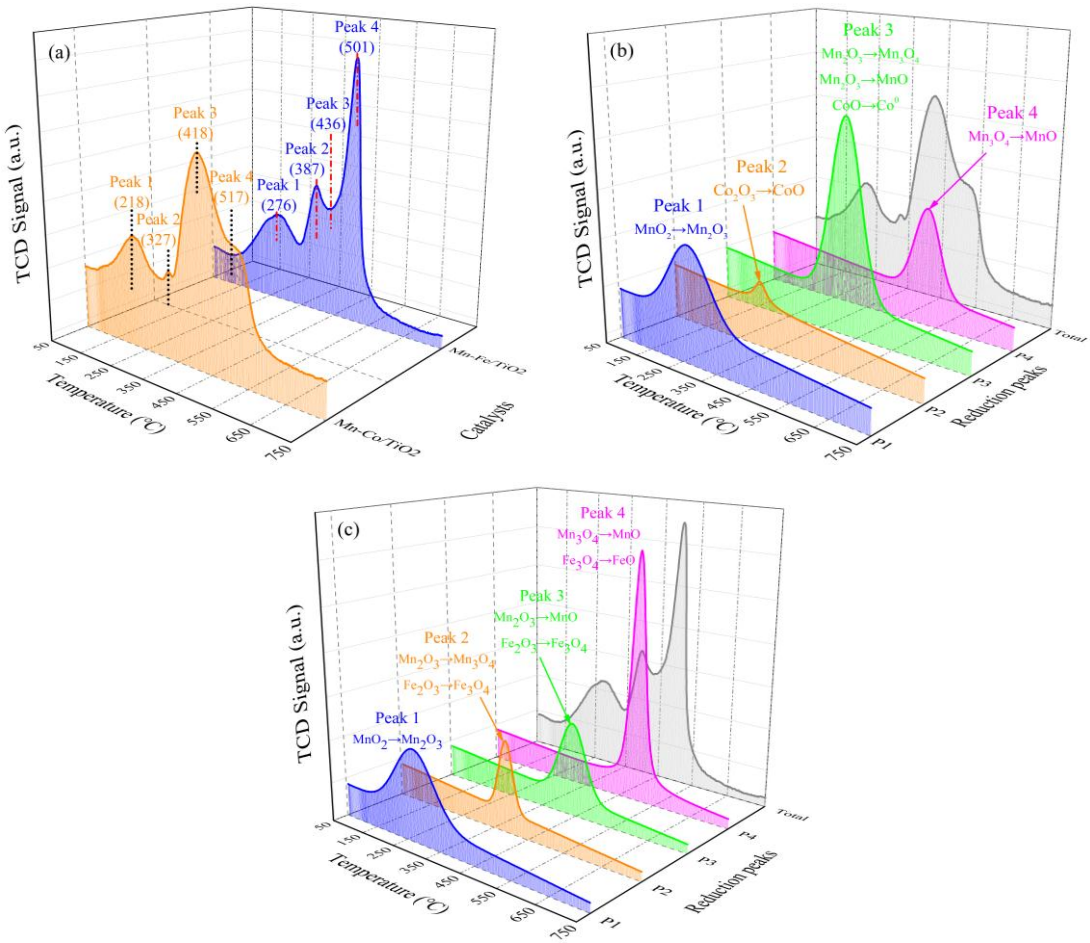

Figure 3. H_2-TPR profiles of Mn−Co/TiO_2 and Mn−Fe/TiO_2 nanocatalysts: (**a**) Total H_2-TPR curves; (**b**) Multi-peaks Gaussian fitting for Mn−Co/TiO_2 nanocatalyst; (**c**) Multi-peaks Gaussian fitting for Mn−Fe/TiO_2 nanocatalyst.

In comparison, the peak intensions and the reduction temperatures of the Mn−Fe/TiO_2 nanocatalyst were evidently different from that of the Mn−Co/TiO_2 sample. The peak of MnO_2 reducing to Mn_2O_3 weakened remarkably and shifted to higher temperature (276 °C). There were wide joint peaks (Peak 2 and Peak 3) at temperature of 330–530 °C, which were ascribed to the coinstantaneous reduction processes of Mn_2O_3 to Mn_3O_4 and Fe_2O_3 to Fe_3O_4. It was proposed that the majority of Fe_2O_3 was reduced at around 380 °C, which located at effortlessly reducible sites in the form of oligomeric clusters, nanoparticles or isolated ions [33]. After the majority of Fe_2O_3 reduction, there was a small quantity of residual Fe_2O_3 reducing to Fe_3O_4 at the higher temperature [34]. The dominating peak (Peak 4), at around 501 °C, was assigned to the overlapped peaks of Mn_3O_4 to MnO and Fe_3O_4 to FeO. Figure 4 provided a graphical representation of the reduction process, in which each active component embodied qualitatively [1,35]. In these two kinds of nanocatalysts, Mn−Co/TiO_2 sample displayed the higher low-temperature reducibility and exhibited a noticeable medium temperature reduction peak at the same time, which manifested the higher oxidation states of manganese ion (Mn^{4+} and Mn^{3+}) constituted the dominating phase [31].

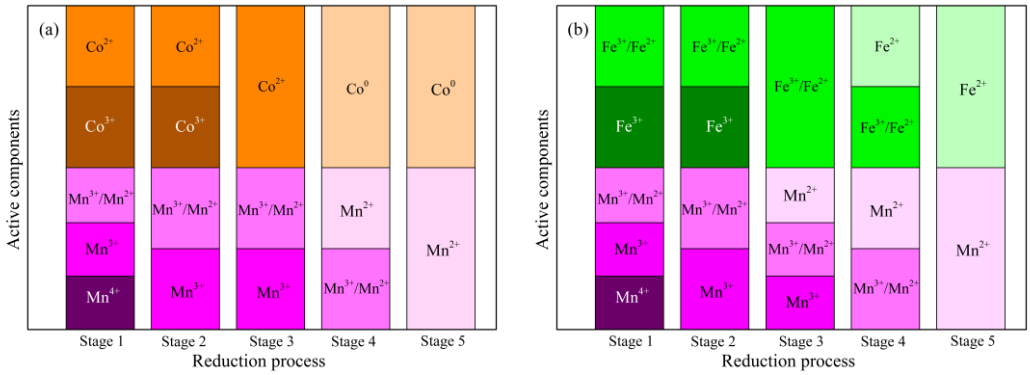

Figure 4. The qualitative component states of active elements during reduction process.

According to Table 2, the total H_2 consumption of Mn−Co/TiO_2 nanocatalyst was 4.43 mmol·g^{-1} much larger than that of Mn−Fe/TiO_2 sample. Meanwhile, the starting reduction peak temperature of Mn−Co/TiO_2 nanocatalyst was at 218 °C lower than that of Mn−Fe/TiO_2, which was regarded as an important factor influencing the reducibility. It was believed that the catalyst performed superior catalytic ability at low temperatures as the reduction peaks arising in lower temperature regions [1].

2.1.5. Ammonia Adsorption Properties

The acid capacity of the Mn−Co/TiO_2 and Mn−Fe/TiO_2 nanocatalysts was measured by NH_3-TPD test, which was another crucial factor effecting the catalyst performance in SCR process [36]. The results were exhibited in Figure 5 and Table 3, respectively. The NH_3-TPD curves for the Mn−Co/TiO_2 and Mn−Fe/TiO_2 nanocatalysts were ascribed to four desorption peaks of chemisorbed NH_3 with the temperature rising from 150 °C to 750 °C. For Mn−Fe/TiO_2 nanocatalyst, the first NH_3 desorption peak occurred at around 209 °C, attributed to NH_3 desorption from weak acid sites, which was too feeble to bound NH_3 steadily in the gas mixture during SCR process [36]. Peak 2 and peak 3 were combined from 398 °C to 585 °C, which were attributed to the medium strong acid sites on the nanocatalyst surface. Peak 4, at around 649 °C, was assigned to the strong acid sites, which were regarded as abundant Lewis acid sites adsorbing a great deal of strongly bound NH_3 [37]. In comparation, the NH_3 desorption results of the Mn−Co/TiO_2 nanocatalyst exhibited better acidity capacity at medium and high temperatures. However, there was an undesired temperature shift to higher temperature occurred in the meantime. For Mn−Co/TiO_2 sample, the desorption temperature of weak acid sites, medium strong acid sites and strong acid sites were 276 °C (Peak 1), 402 °C (Peak 2), 587 °C (Peak 3), and 653 °C (Peak 4), respectively. It was obvious that the medium strong acid sites and the strong acid sites were enriched in the Mn−Co/TiO_2 sample, which were positive to form more abundant Brønsted acid sites and Lewis acid sites promoting NH_3 adsorption on the nanocatalyst surface [38,39].

Table 3. Quantitative analysis of NH_3-TPD profiles.

Samples	Temperature (°C) / NH_3 composition (mmol·g^{-1})				
	Peak 1	**Peak 2**	**Peak 3**	**Peak 4**	**Total**
Mn−Co/TiO_2	276/0.11	402/0.49	587/0.52	653/0.32	−/1.44
Mn−Fe/TiO_2	209/0.14	398/0.24	585/0.39	649/0.20	−/0.97

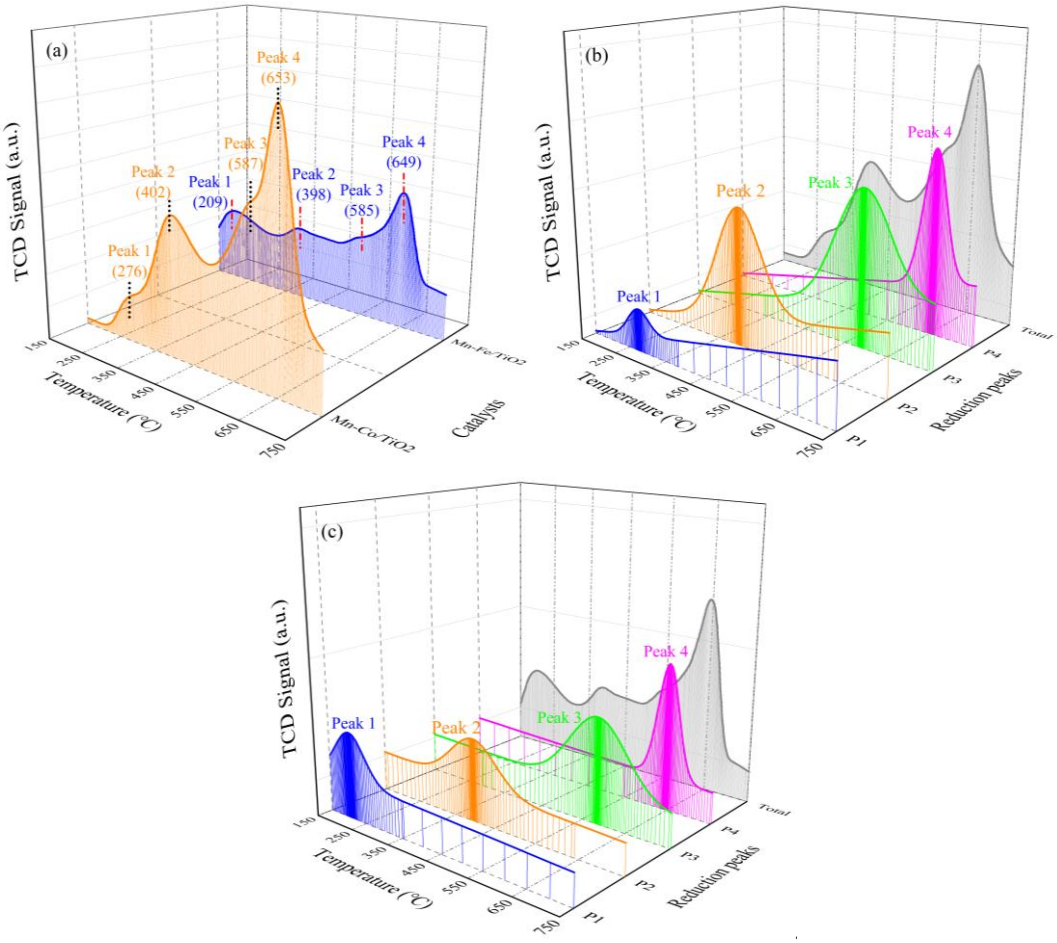

Figure 5. NH_3-TPD profiles of Mn−Co/TiO_2 and Mn−Fe/TiO_2 nanocatalysts: (**a**) Total NH_3-TPD curves; (**b**) Multi-peaks Gaussian fitting for Mn−Co/TiO_2 nanocatalyst; (**c**) Multi-peaks Gaussian fitting for Mn−Fe/TiO_2 nanocatalyst.

The quantitative comparation of the total acid capacity between the Mn−Co/TiO_2 and Mn−Fe/TiO_2 nanocatalysts was performed and summarized in Table 3. The Mn−Co/TiO_2 sample achieved larger total NH_3 desorption of 1.44 mmol·g^{-1} than Mn−Fe/TiO_2, which further confirmed the superior enhancement of $MnCoO_x$ on the surface acidity than $MnFeO_x$. Although the Mn−Fe/TiO_2 sample generated weak acid sites at the lower temperature, the NH_3 desorption on the weak acid sites was only 0.14 mmol·g^{-1}, which was too little to offer enough NH_3 for SCR process. However, it was reported that NH_3 could restrain the adsorption and activation of NO onto the active sites on catalyst surface via the undesirable electron transfer between the adsorbed NH_3 and the metal sites [40]. Consequently, the excessive adsorbed NH_3 could inhibit SCR reactions. Therefore, the surface acidity properties of the Mn−Co/TiO_2 and Mn−Fe/TiO_2 nanocatalysts were bound up with their reducibility properties.

2.1.6. Oxidation States of Active Species

In order to better understand the oxidation states and the atomic concentrations of active species on the surface of Mn−Co/TiO_2 and Mn−Fe/TiO_2 nanocatalysts, the XPS spectra of Ti 2*p*, Mn 2*p*, Co 2*p*, Fe 2*p*, and O 1 *s* were tested and numerically analyzed by Gaussian fitting, respectively, as shown in Figure 6. The binding energy and atomic concentration of each element was summarized in Table 4.

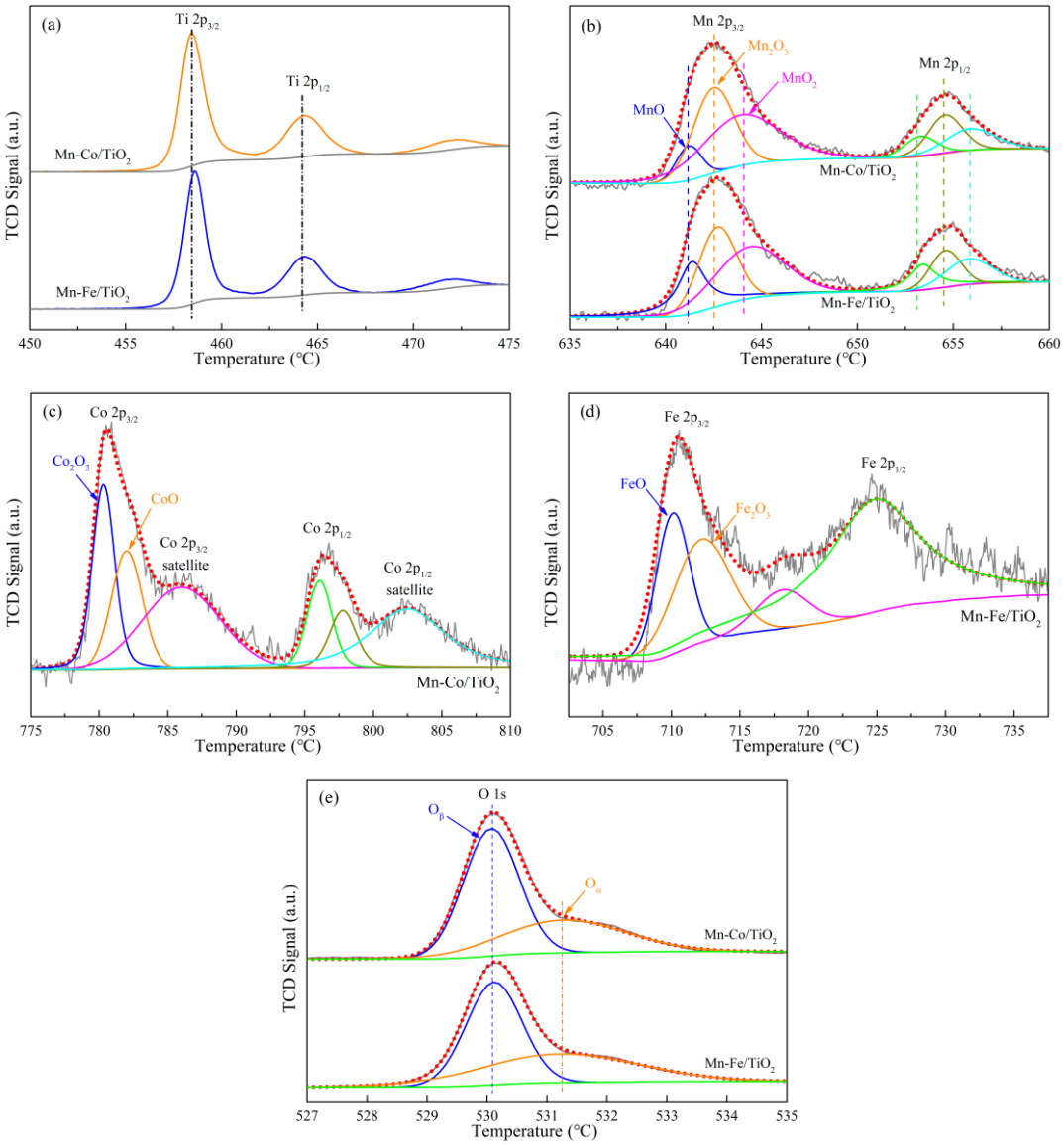

Figure 6. XPS analysis of Mn−Co/TiO_2 and Mn−Fe/TiO_2 nanocatalysts: (**a**) XPS spectra for Ti 2*p*; (**b**) XPS spectra for Mn 2*p*; (**c**) XPS spectra for Co 2*p*; (**d**) XPS spectra for Fe 2*p*; (**e**) XPS spectra for O 1*s*.

Table 4. Surface atomic compositions of the catalysts determined by XPS.

Samples	Binding Energy (eV) / Atomic Composition (%)								
	Mn			Fe		Co		O	
	Mn^{2+}	Mn^{3+}	Mn^{4+}	Fe^{2+}	Fe^{3+}	Co^{2+}	Co^{3+}	O_α	O_β
Mn−Co/TiO_2	641.2/ 13.8	642.6/ 39.4	644.1/ 46.8	-/-	-/-	779.6 39.3	782.1/ 60.7	531.4/ 33.7	530.3/ 66.3
Mn−Fe/TiO_2	641.4/ 21.3	642.8/ 38.5	644.6/ 40.2	709.6/ 43.4	711.7/ 56.6	-/-	-/-	531.6/ 28.2	530.3/ 71.8

As shown in Figure 8a, the XPS spectrum of Ti 2*p* was consisted of two characteristic peaks, attributed to Ti $2p_{1/2}$ at around 464.3 eV and Ti $2p_{3/2}$ at about 458.7 eV, respectively [41]. It was obvious that Ti^{4+} ion was stabilized on the catalyst surface and appeared as the dominating state in the nanocatalysts of Mn−Co/TiO_2 and Mn−Fe/TiO_2. The XPS spectra of Mn 2*p* was composed of Mn $2p_{1/2}$ peak at about 653 eV and Mn $2p_{3/2}$ peak at around 642 eV [42], as exhibited in Figure 6b. The Mn $2p_{3/2}$ peak could be further split into three peaks for Mn^{2+} at 641.2 ± 0.3 eV, Mn^{3+} at 642.6 ± 0.2 eV,

and Mn^{4+} at 644.1 ± 0.5 eV, respectively, according to the multi-peaks Gaussian fitting results [43]. It is evidently difficult to distinguish the three valence states of manganese in MnO_x with the binding energy difference value less than 3.7 eV. For accurate comparison of the atomic concentration of Mn^{n+} on the surface of Mn−Co/TiO_2 and Mn−Fe/TiO_2 nanocatalysts, a quantitative analysis was performed according to the integral area under every divided peak, as exhibited in Table 4. It was widely accepted that the catalytic ability of MnO_x ranked as: MnO_2 > Mn_2O_3 > Mn_3O_4 [12,22,30]. The abundant MnO_2 generated on the nanocatalyst surface was beneficial to SCR reactions [5]. As listed in Table 4, the major amount of manganese in both Mn−Co/TiO_2 and Mn−Fe/TiO_2 nanocatalysts was Mn^{4+}. Meanwhile, the Mn^{4+}/Mn^{n+} atomic composition was 46.8 % in Mn−Co/TiO_2 sample higher than that of 40.2 % in Mn−Fe/TiO_2 sample, generating more lattice oxygen and plenty of oxygen vacancy on the catalyst surface [1], which was regarded as the main reason for higher reducibility properties of Mn−Co/TiO_2 sample as discussed above.

In Co 2*p* spectrum of Mn−Co/TiO_2 nanocatalyst, the two individual peaks were attributed to Co $2p_{1/2}$ at about 796.5 eV and Co $2p_{3/2}$ at around 780.6 eV, respectively. Both of these two main peaks had satellite peaks at 803.1 eV and 786.8 eV, correspondingly, as shown in Figure 6c. The gentler and broader satellite peaks appeared at relatively higher binding energy, which were introduced by the metal-to-ligand electron transfer or the shakeup process of cobalt in its high spin state. However, this shakeup process was only observed with the high spin state of Co^{2+} ion, but did not appear with the diamagnetic low-spin Co^{3+} ion [13]. The intense peak of Co $2p_{3/2}$ was composed of two overlapped peaks, one attributed to Co^{3+} seated at about 780.0 eV and the other ascribed Co^{2+} and located at around 781.6 eV. These two distinguishing peaks indicated the co-occurrence of cobalt in +2 and +3 valence states on the Mn−Co/TiO_2 nanocatalyst surface. There was a dynamic equilibrium sustained on the nanocatalyst surface with the electron transfer between Mn and Co ions during the catalytic oxidation process, expressed as $Co^{3+} + Mn^{3+} \leftrightarrow Co^{2+} + Mn^{4+}$ [44]. Moreover, Co^{3+} species were exhibited as the major atomic concentration of 60.7%, which were at the comparatively higher valence state of Co^{n+} generating vast anionic defects, forming abundant surface oxygen and facilitating adsorption and oxidation during SCR process [45].

In Fe 2*p* spectra of the Mn−Fe/TiO_2 nanocatalyst, as shown in Figure 6d, the two main peaks were ascribed to Fe $2p_{1/2}$ at about 724 eV and Fe $2p_{3/2}$ at around 710 eV. There was a satellite peak at 718.3 eV assigned to Fe^{3+} in Fe_2O_3 [46]. The XPS spectra of Fe $2p_{3/2}$ was composed of two characteristic peaks, ascribed to Fe^{3+} at around 711.6 eV and Fe^{2+} at about 709.6 eV, which meant these two kinds of Fe^{n+} coexisted on the surface of the Mn−Fe/TiO_2 nanocatalyst. It was proposed that the promotion effect between manganese and iron was attributed to the electron transfer in the redox reaction: $Mn^{3+} + Fe^{3+} \leftrightarrow Mn^{4+} + Fe^{2+}$ [47].

The O 1 *s* spectrum of Mn−Co/TiO_2 and Mn−Fe/TiO_2 nanocatalysts were compared in Figure 6e, which was composed of the chemisorbed oxygen peak at 531.2–531.6 eV (O_α) and the lattice oxygen peak at 530.2–530.3 eV (O_β). According to the curve-fitting results, the binding energy of O_α shifted to higher values from 531.4 eV in Mn−Co/TiO_2 sample to 531.6 eV in Mn−Fe/TiO_2 sample. Meanwhile, the similar changes happened to the binding energy of O_β. It was believed that the chemisorbed oxygen (O_α) was the most active oxygen species owing to its high mobility [48]. On the surface of Mn−Co/TiO_2 nanocatalyst, the atomic concentration of O_α reached 33.7% much higher than that of Mn−Fe/TiO_2 sample, which was regarded as another reason for its superior redox ability.

2.2. Catalytic Performance

Figure 7 exhibited the NO conversion and catalytic selectivity over Mn−Co/TiO_2 and Mn−Fe/TiO_2 nanocatalysts. It can be seen that the NO conversion improved conspicuously with the temperature increasing from 25 °C to 250 °C. For both Mn−Co/TiO_2 and Mn−Fe/TiO_2 nanocatalysts, the satisfactory conversion (>90%) was obtained above 150 °C. Meanwhile, the Mn−Ce/TiO_2 nanocatalyst exhibited higher catalytic activity than the Mn−Fe/TiO_2 sample within the temperature range of 50–175 °C. Furthermore, the catalytic selectivity of Mn−Ce/TiO_2 nanocatalyst was higher

than that of Mn−Fe/TiO_2 within 75–250 °C. Therefore, both the catalytic activity and the catalytic selectivity over Mn−Co/TiO_2 were remarkably improved compared to Mn−Fe/TiO_2, potentially due to the interaction between manganese and cobalt stronger than that between manganese and iron, which enhanced the generation of Brønsted acid sites and Lewis acid sites on the nanocatalyst surface, resulting in promoting Langmuir–Hinshelwood mechanism reactions and Eley-Rideal mechanism reactions, simultaneously [49].

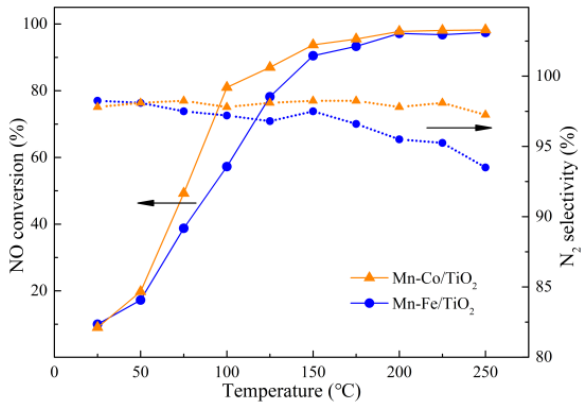

Figure 7. Catalytic performance of Mn−Co/TiO_2 and Mn−Fe/TiO_2 nanocatsalysts.

2.3. Reaction Kinetic Study

It was proposed that both the Langmuir–Hinshelwood mechanism and the Eley–Rideal mechanism contributed to the SCR reactions over nanostructured Fe-Mn oxides [36]. According to Langmuir-Hinshelwood mechanism, the SCR reactions over Mn−Co/TiO_2 and Mn−Fe/TiO_2 nanocatsalysts could be approximately described as:

$$M^{n+} = O + NO\,(ad) \rightarrow M^{(n-1)+}-O-NO \tag{2}$$

$$M^{(n-1)+}-O-NO + NH_3(ad) \rightarrow M^{(n-1)+}-O-NO-NH_3 \rightarrow M^{(n-1)+}-OH + N_2 + H_2O \tag{3}$$

$$M^{(n-1)+}-O-NO + O_2 \rightarrow M^{(n-1)+}-O-NO_2 \tag{4}$$

$$M^{(n-1)+}-O-NO + NH_3(ad) \rightarrow M^{(n-1)+}-O-NO_2-NH_3 \rightarrow M^{(n-1)+}-OH + N_2O + H_2O \tag{5}$$

$$M^{(n-1)+}-OH + O_2 \rightarrow M^{n+}= O + H_2O \tag{6}$$

The adsorbed NO(ad) was oxidized by M^{n+} (Mn^{4+}, Mn^{3+}, Co^{3+}, Fe^{3+}) on the nanocatalyst surface to form NO_2^- (Reaction 2). The NO_2^- reacted with adsorbed NH_3(ad) to generate NH_4NO_2 and decomposed to N_2 and H_2O, subsequently (Reaction 2). In the meantime, an undesired oxidization reaction occurred on NO_2^- which was oxidized to NO_3^- under O_2 (Reaction 4). The formed NO_3^- reacted with adsorbed NH_3(ad) to generate NH_4NO_3 and further decomposed to N_2O and H_2O (Reaction 5). Finally, the active species $M^{(n-1)+} - OH$ was oxidized by O_2 to regenerate $M^{n+}= O$ (Reaction 6).

According to the Eley-Rideal mechanism, the SCR reactions over Mn−Co/TiO_2 and Mn−Fe/TiO_2 nanocatsalysts could be described as:

$$M^{n+}= O + NH_3(ad) \rightarrow M^{(n-1)+}-OH + NH_2(ad) \tag{7}$$

$$NH_2(ad) + NO \rightarrow N_2 + H_2O \tag{8}$$

The adsorbed NH_3(ad) on the nanocatalyst surface was activated by M^{n+} to generate NH_2 (Reaction 7). Then, the NH_2 reacted with NO to form N_2 and H_2O (Reaction 8).

However, in addition to the main Eley-Rideal mechanism reactions, undesirable side reactions occurred on the active species of $M^{n+}= O$.

$$M^{n+}{=}\ O + NH_2(ad) \rightarrow M^{(n-1)+}{-}OH + NH(ad) \tag{9}$$

$$M^{n+}{=}\ O + NH(ad) + NO \rightarrow M^{(n-1)+}{-}OH + N_2O \tag{10}$$

$$M^{n+}{=}\ O + NH(ad) + O_2 \rightarrow M^{(n-1)+}{-}OH + NO \tag{11}$$

The activated NH_2(ad) formed in Reaction 7 was further oxidized to NH(ad) over $M^{n+}{=}\ O$. Then NH(ad) reacted with NO to form N_2O or react with O_2 to generate NO.

According to Reactions 3 and 8, the kinetic equations of N_2 formation rates via the Langmuir-Hinshelwood mechanism and the Eley-Rideal mechanism could be described as:

$$\begin{aligned} k_{scr} = \frac{d[N_2]}{dt} &= \frac{d[N_2]}{dt}\Big|_{LH} + \frac{d[N_2]}{dt}\Big|_{ER} = -\frac{d\left[M^{(n-1)+}{-}O{-}NO{-}NH_3\right]}{dt}\Big|_{LH} - \frac{d[NH_2(ad)]}{dt}\Big|_{ER} \\ &= k_3\left[M^{(n-1)+}{-}O-NO-NH_3\right] + k_8[NH_2(ad)][NO] \end{aligned} \tag{12}$$

where k_3 and k_8 were the kinetic constants of Reactions 3 and 8, $\left[M^{(n-1)+}{-}O-NO-NH_3\right]$, $[NH_2(ad)]$, and [NO] were the concentrations of NH_4NO_2, NH_2(ad), and NO, respectively. When the reactions above reached stable conditions, the concentrations of NH_4NO_2 and NH_2(ad) on the surface of Mn−Co/TiO_2 and Mn−Fe/TiO_2 nanocatalysts could be regarded as constants without connecting with the gaseous concentrations of NH_3 and NO [50]. Therefore, the SCR reaction rate was in a linear relationship with NO concentration as exhibited in Equation (13), the slope and the intercept could be obtained from the linear regression in Figure 8, as listed in Table 5.

$$k_{scr} = k_{SCR-LH} + k_{SCR-ER}[NO] \tag{13}$$

$$k_{SCR-LH} = k_3\left[M^{(n-1)+}{-}O-NO-NH_3\right] \tag{14}$$

$$k_{SCR-ER} = k_8[NH_2(ad)] \tag{15}$$

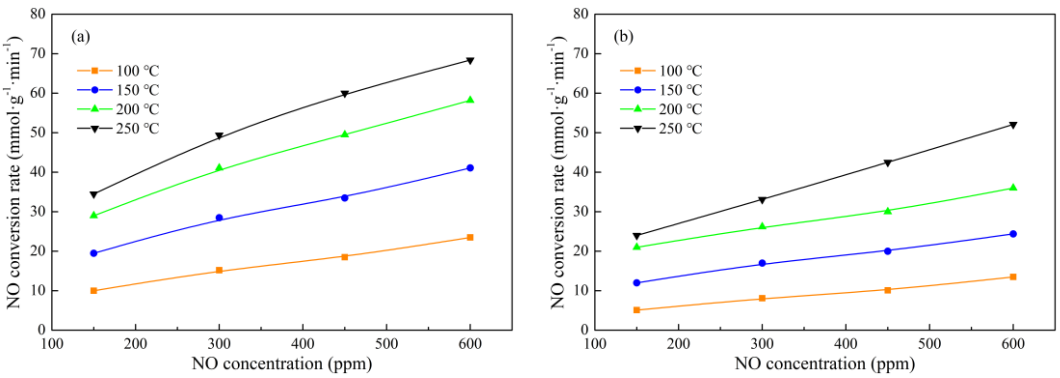

Figure 8. Effect of NO concentration on selective catalytic reduction (SCR) reaction rate.

Table 5. Reaction kinetic constants of NO reduction.

Sample	Temperature (°C)	$k_{SCR\text{-}ER}/10^6$	$k_{SCR\text{-}LH}$	R^2	k_{SCR} [a]
Mn−Co/TiO_2	100	0.029	5.75	0.993	23.5
	150	0.046	13.25	0.994	41.1
	200	0.064	20.50	0.988	58.2
	250	0.075	25.01	0.984	68.4
Mn−Fe/TiO_2	100	0.018	2.35	0.989	13.5
	150	0.027	8.25	0.990	24.4
	200	0.033	16.01	0.991	36.0
	250	0.062	14.50	0.998	52.1

[a] [NO] = [NH_3] = 600 ppm.

2.4. Thermodynamic Calculation

The standard thermodynamic characteristics of the chemical individual species of M_xO_y and M in crystalline states, as well as NH_3, N_2 and H_2O in gaseous states, were listed in Table 6. The oxidative capacities of M_xO_y were evident according to the reliable standard thermodynamic parameters, which was a convincing support for investigating the roles of M_xO_y in NH_3-SCR process. The Gibbs free energies for the reactions between M_xO_y species and ammonia were calculated for estimating their oxidative capacities according to Equation (16), displayed in Table 7. In order to discuss the reaction mechanism conveniently, simplifying assumptions were introduced as follows. Only the kind of main oxidation state was considered in the thermodynamic calculation, although there were several kinds of oxidation states for each M_xO_y [51]. Meanwhile, it was assumed that every M_xO_y was reduced into metal, although the metallic oxide in the high-oxidation state was reduced step-by-step in the actual process. It had been proved that the entropy of metals would vary drastically as the metal physical states transforming [52]. Furthermore, the transformation could bring about the changes of the straight slope of the temperature–Gibbs free energy curve which was named Ellingham diagrams. The Ellingham diagrams were a particular graphical form of the principle that the thermodynamic feasibility of a reaction depends on the Gibbs free energy change ($\Delta_f G^0$), which could be calculated using Equation (16), where $\Delta_f H^0$ was the enthalpy change and ΔS^0 was the entropy change under standard state.

$$\Delta_f G^0 = \Delta_f H^0 - T\Delta S^0 \quad (16)$$

Table 6. Standard thermodynamic properties of M_xO_y [7,53–55].

	C_p J mol^{-1} K	$\triangle_f H^0$ kJ mol^{-1}	S^0 J mol^{-1} K	$\triangle_f G^0$ kJ mol^{-1}
Mn	26.3	0.0	32.0	-
MnO	45.4	−385.2	59.7	−362.9
Mn_3O_4	139.7	−1387.8	155.6	-1283.2
Mn_2O_3	107.7	−959.0	110.5	−881.1
MnO_2	54.1	−520.0	53.1	−465.1
Co	24.8	0.0	30.0	-
CoO	55.2	−237.9	53.0	−214.2
Co_3O_4	123.4	−891.0	102.5	−774.0
Fe	25.1	0.0	27.3	-
FeO	-	−272.0	-	-
Fe_3O_4	143.4	−1118.4	146.4	−1015.4
Fe_2O_3	103.9	−824.2	87.4	−742.2
NH_3	-	45.9	192.8	-
N_2	29.1	0.0	191.6	-
H_2O (g)	33.6	−241.8	188.8	−228.6

Table 7. Gibbs free energy for the reaction between M_xO_y and NH_3 under different temperatures.

Substance	$\triangle_f G$ /kJ					
	298 K	**323 K**	**373 K**	**423 K**	**473 K**	**523 K**
MnO_2	−46.25	−49.09	−54.77	−60.45	−66.12	−71.80
Mn_3O_4	42.00	39.27	33.81	28.34	22.88	17.42
MnO	84.06	81.65	76.83	72.01	67.19	62.37
Co_3O_4 [a]	−85.71	−88.74	−94.79	−100.84	−106.89	−112.94
CoO	−64.64	−67.17	−72.22	−77.28	−82.34	−87.39
Fe_2O_3	−31.40	−34.23	−39.89	−45.55	−51.21	−56.87
Fe_3O_4	−24.99	−27.69	−33.09	−38.49	−43.89	−49.29

[a] Co_3O_4 was regard as the compound of Co_2O_3 and CoO.

The Ellingham diagram plotted $\Delta_f G$ for each oxidation reaction as a function of temperature. In order to compare different reactions, all $\Delta_f G$ values referred to the same quantity of oxygen, chosen as one mole O (1/2 mol O_2) [53], as shown in Equation (17)

$$\frac{1}{y}M_xO_y + \frac{2}{3}NH_3 \rightarrow \frac{x}{y}M + \frac{1}{3}N_2 + H_2O \tag{17}$$

According to Equations (16) and (17), the redox reactions that happened between M_xO_y and NH_3 were discussed under thermodynamic calculation, assuming that the enthalpy, entropy, and Gibbs free energy remained unchanged with temperature. The $\Delta_f G$ in Table 7 for each kind of M_xO_y was calculated in order to estimate its oxidative capacities and gain semiquantitative conclusions. Meanwhile, this research just focused on the catalytic performance and reaction mechanism of cobalt and iron doped in the Mn/TiO_2 nanocatalysts, so that only one M_xO_y was different at a time. The negative $\Delta_f G$ values for Co_3O_4 (the compound of Co_2O_3 and CoO) and Fe_2O_3 indicated M_xO_y was effective for the oxidative abstraction of the hydrogen from adsorbed ammonia [7].

The Ellingham diagrams for the Gibbs free energy of reactions between M_xO_y and NH_3 with the reaction temperature rising was displayed in Figure 9. As the $\triangle_f G$ was negative ($\triangle_f G < 0$), the reaction took place more easily. On the contrary, the reaction would happen at higher temperature or would not happen if the $\triangle_f G$ was positive ($\triangle_f G > 0$). Under the same reaction temperature, the order of temperature−Gibbs free energy for the reaction between M_xO_y and NH_3 is as follows: Co_3O_4 (compound of Co_2O_3 and CoO) < CoO < Fe_2O_3 < Fe_3O_4 (only considering the doping transition metals). These results were exactly consistent with the NH_3-SCR performance and almost coincided with the data of the nanostructure characterization, as discussed above, which demonstrated the simplifying assumptions used in the thermodynamic calculations was reasonable. However, the activity of MnO_x exhibited in Ellingham Diagrams was not in well accord with the reducibility properties, which might be on account of positive kinetics or simplifying assumptions during the thermodynamic calculations [51,53]. It manifested that MnO_x, as the dominate phase in nonacatalysts of $Mn-Co/TiO_2$ and $Mn-Fe/TiO_2$, was activated by the doping of cobalt or iron. A large number of researches had been carried out focusing on optimizing catalysts via doping transition metals in order to enhance NO catalytic conversion remarkably. Based on the thermodynamic study, Ellingham diagrams would provide a novel insight for developing catalysts doped proper metal oxides with higher NH_3-SCR activity.

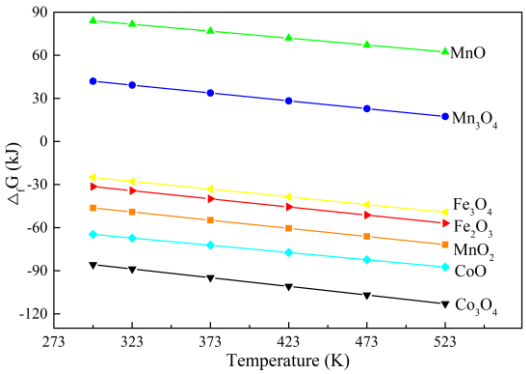

Figure 9. Temperature−Gibbs free energy curve for the reaction between M_xO_y and NH_3.

3. Materials and Methods

3.1. Catalysts Preparation

The noncatalysts of Mn−Co/TiO_2 and Mn−Fe/TiO_2 were prepared by hydrothermal method. $Co(CH_3COO)_2{\cdot}4H_2O$ (analytical pure 99.9%, Kermel, Tianjin, China) and $Fe(NO_3)_3{\cdot}9H_2O$ (analytical pure 99.9%, Sinopharm, Shanghai, China) were used as the precursors of CoO_x and FeO_x, respectively. The aqueous solution of $Mn(NO_3)_2$ (analytical pure 50.0%, Sinopharm, Shanghai, China) was used as the precursors of MnO_x. The tetrabutyl titanate was introduced as the precursors of anatase TiO_2 to support the bimetals oxides. The precursors were added into deionized water at room temperature. One-hundred fifty mL glycol was added into the above mixture with magnetic stirring continuously to regulate the reaction rate of hydrothermal reaction. Then the homogeneous solution was heat at 180 °C for 8 h in a Teflon-lined stainless steel autoclave. After that, tetrabutyl titanate was added into the solution and reheated in the autoclave at 180 °C for 3 h. The precipitate was obtained by reduplicative centrifugation and wash. In the end, the nanocatalysts were dried at 150 °C for 12 h and calcined in air at 500 °C for 4 h. The nanocatalyst was denoted as Mn−Co/TiO_2 and Mn−Fe/TiO_2 with the molar ratios of Mn:M:Ti = 2:1:7.

3.2. Catalysts Characterization

The advanced microstructural image data and the surface element contents of the nanocatalysts was achieved by a high resolution transmission electron microscope JEOL JEM-2010 (Japan electronics corporation, Tokyo, Japan) combined with EDS. The Maxon Tristar II 3020 micropore-size analyzer (Maxon, Chicago, IL, USA) was used for testing N_2 adsorption isotherms of the prepared nanocatalysts at −196 °C. The surface areas and the pore-size distributions of the nanocatalysts were measured after the nanocatalysts degassing in vacuum at 350 °C for 10 h. BET plot linear portion was used to determine the nanocatalysts specific surface areas, and the desorption branch with Barrett–Joyner–Halenda (BJH) formula was introduced to calculate the pore-size distributions. The XRD data was captured by a Bruker D8 advance analyzer (Bruker, Frankfurt, Germany) with Mo K_α radiation, diffraction intensity from 10° to 90°, point counting time of 1 s and point counting step of 0.02°. The element phases contained in the nanocatalysts were distinguished by comparing characteristic peaks presented in the XRD patterns with the International Center for Diffraction Data (ICDD). H_2-TPR and NH_3-TPD tests were performed with a Micromeritics Autochem II 2920 chemical adsorption instrument (Micromeritics, Houston, TX, USA). During H_2-TPR experiment, nanocatalysts were pretreatment in He at 400 °C for 1 h, and then cooled to environment temperature in H_2 and He gas mixture at 30 mL/min. The test temperature range of H_2 consumptions was from 50 °C to 850 °C with the heating rate of 10 °C/min. The operating process of NH_3-TPD test was similar to that of H_2-TPR test with NH_3 replacing H_2. XPS analysis was performed on a Thermo ESCALAB 250XI (Thermo Fisher, Boston, MA, USA) with

pass energy 46.95 eV, Al K_α radiation 1486.6 eV, X-ray source 150 W, and binding energy precision ±0.3 eV. The C 1 *s* line at 284.6 eV was measured as a reference.

3.3. Catalytic Performance Tests

The catalytic properties of the Mn−Co/TiO_2 and Mn−Fe/TiO_2 nanocatalysts were tested on a fixed-bed quartz tube reactor including a tube furnace and a temperature control unit, as shown in Figure 10. The mass of the catalyst was 250 mg with the particle diameter of 40–60 mesh. During NO conversion test, 5 mL nanocatalyst with the particle diameter of 40–60 mesh was used under the total flow rate of 2000 mL/min, corresponding to the gas hourly space velocity (GHSV) of 24,000 h^{-1}. The feed gas contained 300 ppm NO, 300 ppm NH_3, 5% O_2, and N_2 as balance gas. During reaction kinetic study, the reaction conditions were NO 150–600 ppm, NH_3 600 ppm, O_2 5%, catalyst mass of 200 mg, total flow rate at 4000 mL/min, and GHSV at 1 200 000 $cm^3 \cdot g^{-1} \cdot h^{-1}$. The concentrations of NO, N_2O, and NH_3 in the outlet were continually monitored using German MRU MGA-5 analyzer (MRU, Berlin, Germany) joint with an external special detector for N_2O and NH_3. The NO conversion was calculated according to Equation (18). The N_2 selectivity was calculated by the concentrations of N_2O and NO, as show in Equation (19). Each experiment was repeated three times to confirm the results accuracy.

$$\text{NO conversion} = \left(\frac{[\text{NO}]_{\text{in}} - [\text{NO}]_{\text{out}}}{[\text{NO}]_{\text{in}}}\right) \times 100\% \tag{18}$$

$$\text{N}_2 \text{ selectivity} = 1 - \frac{2[\text{N}_2\text{O}]_{\text{out}}}{[\text{NO}]_{\text{in}} - [\text{NO}]_{\text{out}}} \times 100\% \tag{19}$$

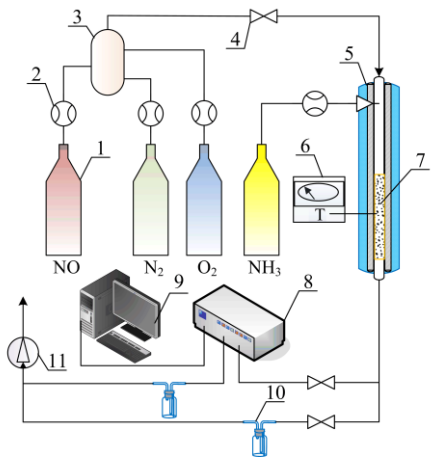

Figure 10. The schematic diagram of SCR experiments. 1, standard gas; 2, mass flowmeter; 3, gas mixer; 4, shutdown valve; 5, resistance furnace; 6, temperature controller; 7, nanocatalysts; 8, flue gas analyzer; 9, record system; 10, gas washing bottle; 11, induced draft fan.

4. Conclusions

The multiple characterizations performed on the Mn−Co/TiO_2 and Mn−Fe/TiO_2 nanocatalysts indicated that the Mn−Co/TiO_2 sample obtained the superior structure characteristics than Mn−Fe/TiO_2 with the surface area increased by 85.3 $m^2 \cdot g^{-1}$, the nanoparticle size reduced by 21.79 nm, the active components distribution improved, and the crystallinity decreased. Meanwhile, these results further confirmed the catalytic property was highly dependent on the phase compositions of the catalysts. The ratios of Mn^{4+}/Mn^{n+} in the Mn−Co/TiO_2 sample was 46.8% higher than that of 40.2% in the Mn−Fe/TiO_2 sample, which demonstrated the better oxidation ability and the larger amount of Bronsted acid sites and Lewis acid sites on the sample surface. Both Mn−Co/TiO_2 and Mn−Fe/TiO_2 nanocatalysts exhibited the satisfactory conversion (>90%) above 150 °C. When compared to the

Mn−Fe/TiO_2 nanocatalyst, the Mn−Ce/TiO_2 sample displayed the preferable catalytic property with higher catalytic activity and stronger selectivity in the temperature range of 75—250 °C. In the meantime, the mechanism and kinetic study showed that Langmuir-Hinshelwood mechanism and Eley-Rideal mechanism reactions contributed to NH_3-SCR catalysis, simultaneously. Under the same test conditions, the NO conversion rate of Mn−Co/TiO_2 nanocatalyst was always higher than that of Mn−Fe/TiO_2 sample. Furthermore, Ellingham Diagrams of Mn−Co/TiO_2 and Mn−Fe/TiO_2 nanocatalysts were in accordance with their catalytic performances, based on the Gibbs free energy calculation of the reactions between ammonia and each kind of active metal oxide. Generally, Mn−Co/TiO_2 nanocatalyst exhibited the better catalytic properties than Mn−Fe/TiO_2 sample according to the comprehensive comparison in this research. The comparison with the insight from structure, performance, kinetics, and thermodynamics might supply a theoretical method to select superior metal oxides for NH_3-SCR.

Author Contributions: Conceptualization, Y.G.; Funding acquisition, Y.G., T.L.; Methodology, Y.G., T.L. Project administration, Y.G.; Writing—original draft, Y.G.; Writing—review & editing, T.L.; Data curation, S.Z., W.J., W.F., H.J.

Funding: This work was supported by Shandong Provincial Science and Technology Development Plan (2011GSF11716), Doctoral research fund project of Shandong Jianzhu university (XNBS1835), Shandong Jianzhu university open experimental project (2018yzkf023, 2018wzkf013), and the Shandong electric power engineering consulting institute science and technology project (37-K2014-33).

Conflicts of Interest: The authors declare no conflict of interest.

References

1. France, L.J.; Yang, Q.; Li, W.; Chen, Z.; Guang, J.; Guo, D.; Wang, L.; Li, X. Ceria modified $FeMnO_x$—Enhanced performance and sulphur resistance for low-temperature SCR of NO_x. *Appl. Catal. B Environ.* **2017**, *206*, 203–215. [CrossRef]
2. Gillot, S.; Tricot, G.; Vezin, H.; Dacquin, J.-P.; Dujardin, C.; Granger, P. Induced effect of tungsten incorporation on the catalytic properties of $CeVO_4$ systems for the selective reduction of NO_x by ammonia. *Appl. Catal. B Environ.* **2018**, *234*, 318–328. [CrossRef]
3. Liu, J.; Li, X.; Zhao, Q.; Ke, J.; Xiao, H.; Lv, X.; Liu, S.; Tadé, M.; Wang, S. Mechanistic investigation of the enhanced NH_3-SCR on cobalt-decorated Ce-Ti mixed oxide: In situ FTIR analysis for structure-activity correlation. *Appl. Catal. B Environ.* **2017**, *200*, 297–308. [CrossRef]
4. Gao, Y.; Luan, T.; Lu, T.; Cheng, K.; Xu, H. Performance of V_2O_5-WO_3-MoO_3/TiO_2 Catalyst for Selective Catalytic Reduction of NO_x by NH_3. *Chin. J. Chem. Eng.* **2013**, *21*, 1–7. [CrossRef]
5. Huang, J.; Huang, H.; Jiang, H.; Liu, L. The promotional role of Nd on Mn/TiO_2 catalyst for the low-temperature NH_3 -SCR of NO_x. *Catal. Today* **2018**, *411*, 338–346. [CrossRef]
6. Zhang, R.; Yang, W.; Luo, N.; Li, P.; Lei, Z.; Chen, B. Low-temperature NH_3-SCR of NO by lanthanum manganite perovskites: Effect of A-/B-site substitution and TiO_2/CeO_2 support. *Appl. Catal. B Environ.* **2014**, *146*, 94–104. [CrossRef]
7. Fang, D.; He, F.; Mei, D.; Zhang, Z.; Xie, J.; Hu, H. Thermodynamic calculation for the activity and mechanism of Mn/TiO_2 catalyst doped transition metals for SCR at low temperature. *Catal. Commun.* **2014**, *52*, 45–48. [CrossRef]
8. Qiu, M.; Zhan, S.; Yu, H.; Zhu, D. Low-temperature selective catalytic reduction of NO with NH_3 over ordered mesoporous $Mn_xCo_{3-x}O_4$ catalyst. *Catal. Commun.* **2015**, *62*, 107–111. [CrossRef]
9. Zhou, C.; Zhang, Y.; Wang, X.; Xu, H.; Sun, K.; Shen, K. Influence of the addition of transition metals (Cr, Zr, Mo) on the properties of MnO_x –FeO_x catalysts for low-temperature selective catalytic reduction of NO_x by Ammonia. *J. Colloid Interface Sci.* **2013**, *392*, 319–324. [CrossRef]
10. Wang, R.; Wu, X.; Zou, C.; Li, X.; Du, Y. NOx Removal by Selective Catalytic Reduction with Ammonia over a Hydrotalcite-Derived NiFe Mixed Oxide. *Catalysts* **2018**, *8*, 384. [CrossRef]
11. Li, W.; Guo, R.-T.; Wang, S.-X.; Pan, W.-G.; Chen, Q.-L.; Li, M.-Y.; Sun, P.; Liu, S.-M. The enhanced Zn resistance of Mn/TiO_2 catalyst for NH_3 -SCR reaction by the modification with Nb. *Fuel Process. Technol.* **2016**, *154*, 235–242. [CrossRef]

12. Gao, F.; Tang, X.; Yi, H.; Chu, C.; Li, N.; Li, J.; Zhao, S. In-situ DRIFTS for the mechanistic studies of NO oxidation over α-MnO_2, β-MnO_2 and γ-MnO_2 catalysts. *Chem. Eng. J.* **2017**, *322*, 525–537. [CrossRef]
13. Hu, H.; Cai, S.; Li, H.; Huang, L.; Shi, L.; Zhang, D. Mechanistic Aspects of deNO_x Processing over TiO_2 Supported Co–Mn Oxide Catalysts: Structure–Activity Relationships and In Situ DRIFTs Analysis. *ACS Catal.* **2015**, *5*, 6069–6077. [CrossRef]
14. Yang, S.; Wang, C.; Li, J.; Yan, N.; Ma, L.; Chang, H. Low temperature selective catalytic reduction of NO with NH_3 over Mn–Fe spinel: Performance, mechanism and kinetic study. *Appl. Catal. B Environ.* **2011**, *110*, 71–80. [CrossRef]
15. Zhang, Y.; Zheng, Y.; Wang, X.; Lu, X. Preparation of Mn–FeO_x/CNTs catalysts by redox co-precipitation and application in low-temperature NO reduction with NH_3. *Catal. Commun.* **2015**, *62*, 57–61. [CrossRef]
16. Gao, Y.; Jiang, W.; Luan, T.; Li, H.; Zhang, W.; Feng, W.; Jiang, H. High-Efficiency Catalytic Conversion of NO_x by the Synergy of Nanocatalyst and Plasma: Effect of Mn-Based Bimetallic Active Species. *Catalysts* **2019**, *9*, 103. [CrossRef]
17. Qiu, L.; Pang, D.; Zhang, C.; Meng, J.; Zhu, R.; Ouyang, F. In situ IR studies of Co and Ce doped Mn/TiO_2 catalyst for low-temperature selective catalytic reduction of NO with NH_3. *Appl. Surf. Sci.* **2015**, *357*, 189–196. [CrossRef]
18. Chen, Y.; Wang, J.; Yan, Z.; Liu, L.; Zhang, Z.; Wang, X. Promoting effect of Nd on the reduction of NO with NH_3 over CeO_2 supported by activated semi-coke: An in situ DRIFTS study. *Catal. Sci. Technol.* **2015**, *5*, 2251–2259. [CrossRef]
19. Wang, X.; Shi, Y.; Li, S.; Li, W. Promotional synergistic effect of Cu and Nb doping on a novel Cu/Ti-Nb ternary oxide catalyst for the selective catalytic reduction of NO_x with NH_3. *Appl. Catal. B Environ.* **2018**, *220*, 234–250. [CrossRef]
20. Yang, S.; Fu, Y.; Liao, Y.; Xiong, S.; Qu, Z.; Yan, N.; Li, J. Competition of selective catalytic reduction and non selective catalytic reduction over MnO_x/TiO_2 for NO removal: the relationship between gaseous NO concentration and N_2O selectivity. *Catal. Sci. Technol.* **2014**, *4*, 224–232. [CrossRef]
21. Wei, L.; Cui, S.; Guo, H.; Ma, X. Study on the role of Mn species in low temperature SCR on MnO_x/TiO_2 through experiment and DFT calculation. *Mol. Catal.* **2018**, *445*, 102–110. [CrossRef]
22. Kapteijn, F.; Singoredjo, L.; Andreini, A.; Moulijn, J.A. Activity and selectivity of pure manganese oxides in the selective catalytic reduction of nitric oxide with ammonia. *Appl. Catal. B Environ.* **1994**, *3*, 173–189. [CrossRef]
23. Gao, Y.; Luan, T.; Zhang, W.; Li, H. The promotional effects of cerium on the catalytic properties of Al_2O_3-supported $MnFeO_x$ for NO oxidation and fast SCR reaction. *Res. Chem. Intermed.* **2019**, *45*, 663–686. [CrossRef]
24. Liu, Z.; Yi, Y.; Zhang, S.; Zhu, T.; Zhu, J.; Wang, J. Selective catalytic reduction of NO_x with NH_3 over Mn-Ce mixed oxide catalyst at low temperatures. *Catal. Today* **2013**, *216*, 76–81. [CrossRef]
25. Li, X.; Zhang, S.; Jia, Y.; Liu, X.; Zhong, Q. Selective catalytic oxidation of NO with O_2 over Ce-doped MnO_x/TiO_2 catalysts. *J. Nat. Gas Chem.* **2012**, *21*, 17–24. [CrossRef]
26. Ma, Z.; Yang, H.; Li, Q.; Zheng, J.; Zhang, X. Catalytic reduction of NO by NH_3 over Fe–Cu–O_x/CNTs-TiO_2 composites at low temperature. *Appl. Catal. A Gen.* **2012**, *427–428*, 43–48. [CrossRef]
27. Shi, Y.; Chen, S.; Sun, H.; Shu, Y.; Quan, X. Low-temperature selective catalytic reduction of NO_x with NH_3 over hierarchically macro-mesoporous Mn/TiO_2. *Catal. Commun.* **2013**, *42*, 10–13. [CrossRef]
28. Gong, P.; Xie, J.; Fang, D.; Han, D.; He, F.; Li, F.; Qi, K. Effects of surface physicochemical properties on NH_3-SCR activity of MnO_2 catalysts with different crystal structures. *Chin. J. Catal.* **2017**, *38*, 1925–1934. [CrossRef]
29. Boningari, T.; Pappas, D.K.; Ettireddy, P.R.; Kotrba, A.; Smirniotis, P.G. Influence of SiO_2 on M/TiO_2 (M = Cu, Mn, and Ce) Formulations for Low-Temperature Selective Catalytic Reduction of NO_x with NH_3: Surface Properties and Key Components in Relation to the Activity of NO_x Reduction. *Ind. Eng. Chem. Res.* **2015**, *54*, 2261–2273. [CrossRef]
30. Luo, S.; Zhou, W.; Xie, A.; Wu, F.; Yao, C.; Li, X.; Zuo, S.; Liu, T. Effect of MnO_2 polymorphs structure on the selective catalytic reduction of NO_x with NH_3 over TiO_2–Palygorskite. *Chem. Eng. J.* **2016**, *286*, 291–299. [CrossRef]
31. Jiang, H.; Wang, C.; Wang, H.; Zhang, M. Synthesis of highly efficient MnO_x catalyst for low-temperature NH_3-SCR prepared from Mn-MOF-74 template. *Mater. Lett.* **2016**, *168*, 17–19. [CrossRef]

32. Meng, D.; Xu, Q.; Jiao, Y.; Guo, Y.; Guo, Y.; Wang, L.; Lu, G.; Zhan, W. Spinel structured CoaMnbOx mixed oxide catalyst for the selective catalytic reduction of NO_x with NH_3. *Appl. Catal. B Environ.* **2018**, *221*, 652–663. [CrossRef]
33. Stanciulescu, M.; Caravaggio, G.; Dobri, A.; Moir, J.; Burich, R.; Charland, J.P.; Bulsink, P. Low-temperature selective catalytic reduction of NO_x with NH_3 over Mn-containing catalysts. *Appl. Catal. B Environ.* **2012**, *123–124*, 229–240. [CrossRef]
34. Kong, F.; Qiu, j.; Liu, H.; Zhao, R.; Zeng, H. Effect of NO/SO_2 on Elemental Mercury Adsorption by Nano-Fe_2O_3. *Korean J. Chem. Eng.* **2010**, *30*, 43–48. [CrossRef]
35. Gao, Y.; Luan, T.; Zhang, M.; Zhang, W.; Feng, W. Structure–Activity Relationship Study of Mn/Fe Ratio Effects on $Mn-Fe-Ce-O_x/\gamma$-Al_2O_3 Nanocatalyst for NO Oxidation and Fast SCR Reaction. *Catalysts* **2018**, *8*, 642. [CrossRef]
36. Zhang, C.; Chen, T.; Liu, H.; Chen, D.; Xu, B.; Qing, C. Low temperature SCR reaction over Nano-Structured Fe-Mn Oxides: Characterization, performance, and kinetic study. *Appl. Surf. Sci.* **2018**, *457*, 1116–1125. [CrossRef]
37. Jin, R.; Liu, Y.; Wu, Z.; Wang, H.; Gu, T. Low-temperature selective catalytic reduction of NO with NH_3 over MnCe oxides supported on TiO_2 and Al_2O_3: A comparative study. *Chemosphere* **2010**, *78*, 1160–1166. [CrossRef]
38. Xiong, Z.-b.; Liu, J.; Zhou, F.; Liu, D.-y.; Lu, W.; Jin, J.; Ding, S.-f. Selective catalytic reduction of NO_x with NH_3 over iron-cerium-tungsten mixed oxide catalyst prepared by different methods. *Appl. Surf. Sci.* **2017**, *406*, 218–225. [CrossRef]
39. Liu, F.; He, H.; Zhang, C.; Shan, W.; Shi, X. Mechanism of the selective catalytic reduction of NO_x with NH_3 over environmental-friendly iron titanate catalyst. *Catal. Today* **2011**, *175*, 18–25. [CrossRef]
40. Fan, X.; Qiu, F.; Yang, H.; Tian, W.; Hou, T.; Zhang, X. Selective catalytic reduction of NO_X with ammonia over Mn–Ce–O_X/TiO_2-carbon nanotube composites. *Catal. Commun.* **2011**, *12*, 1298–1301. [CrossRef]
41. Guan, D.S.; Wang, Y. Synthesis and growth mechanism of multilayer TiO_2 nanotube arrays. *Nanoscale* **2012**, *4*, 2968–2977. [CrossRef] [PubMed]
42. Lu, X.; Shen, C.; Zhang, Z.; Barrios, E.; Zhai, L. Core–Shell Composite Fibers for High-Performance Flexible Supercapacitor Electrodes. *ACS Appl. Mater. Interfaces* **2018**, *10*, 4041–4049. [CrossRef]
43. Wang, C.; Yu, F.; Zhu, M.; Wang, X.; Dan, J.; Zhang, J.; Cao, P.; Dai, B. Microspherical MnO_2-CeO_2-Al_2O_3 mixed oxide for monolithic honeycomb catalyst and application in selective catalytic reduction of NO_x with NH_3 at 50–150 °C. *Chem. Eng. J.* **2018**, *346*, 182–192. [CrossRef]
44. Deng, L.; Ding, Y.; Duan, B.; Chen, Y.; Li, P.; Zhu, S.; Shen, S. Catalytic deep combustion characteristics of benzene over cobalt doped Mn-Ce solid solution catalysts at lower temperatures. *Mol. Catal.* **2018**, *446*, 72–80. [CrossRef]
45. Li, K.; Tang, X.; Yi, H.; Ning, P.; Kang, D.; Wang, C. Low-temperature catalytic oxidation of NO over Mn–Co–Ce–O_x catalyst. *Chem. Eng. J.* **2012**, *192*, 99–104. [CrossRef]
46. Zhang, W.; Wang, F.; Li, X.; Liu, Y.; Liu, Y.; Ma, J. Fabrication of hollow carbon nanospheres introduced with Fe and N species immobilized palladium nanoparticles as catalysts for the semihydrogenation of phenylacetylene under mild reaction conditions. *Appl. Surf. Sci.* **2017**, *404*, 398–408. [CrossRef]
47. Wang, T.; Wan, Z.; Yang, X.; Zhang, X.; Niu, X.; Sun, B. Promotional effect of iron modification on the catalytic properties of Mn-Fe/ZSM-5 catalysts in the Fast SCR reaction. *Fuel Process. Technol.* **2018**, *169*, 112–121. [CrossRef]
48. Marbán, G.; Valdés-Solis, T.; Fuertes, A.B. Mechanism of low-temperature selective catalytic reduction of NO with NH_3 over carbon-supported Mn_3O_4: Role of surface NH_3 species: SCR mechanism. *J. Catal.* **2004**, *226*, 138–155. [CrossRef]
49. Liu, Z.; Zhu, J.; Li, J.; Ma, L.; Woo, S.I. Novel Mn–Ce–Ti Mixed-Oxide Catalyst for the Selective Catalytic Reduction of NO_x with NH_3. *ACS Appl. Mater. Interfaces* **2014**, *6*, 14500–14508. [CrossRef] [PubMed]
50. Xiong, S.; Liao, Y.; Xiao, X.; Dang, H.; Yang, S. Novel Effect of H_2O on the Low Temperature Selective Catalytic Reduction of NO with NH_3 over MnO_x-CeO_2: Mechanism and Kinetic Study. *J. Phys. Chem. C* **2015**, *119*, 4180–4187. [CrossRef]
51. Lu, J.J.; Murray, N.V.; Rosenthal, E. Signed formulas and annotated logics. In *Proceedings of the [1993] Proceedings of the Twenty-Third International Symposium on Multiple-Valued Logic*; Institute of Electrical and Electronics Engineers (IEEE): Piscatville, NJ, USA, 2002; pp. 48–53.

52. Lee, J.D. *A New Concise Inorganic Chemistry*; Van Nostrand Reinhold: Berkshire, UK, 1991; ISBN 0-412-40290-4.
53. Cooksy, A. *Physical Chemistry: Thermodynamics, Statistical Mechanics, and Kinetics*; PEARSON EDUCATION: Boston, MA, USA, 2012; ISBN 0-321-81415-0.
54. Lide, D.R. *CRC Handbook of Chemistry and Physics*, 90th ed.; CRC Press: Boca Raton, FL, USA, 2010; ISBN 978-1439820773.
55. Koebel, M.; Elsener, M. Selective catalytic reduction of NO over commercial $DeNO_x$-catalysts: Experimental determination of kinetic and thermodynamic parameters. *Chem. Eng. Sci.* **1998**, *53*, 657–669. [CrossRef]